Application of Light Reflectance-Transmittance Measurement Method to Reconstruct Geometrical Morphology of Particle Fractal Aggregates

LIU Zhigang[1], *FANG Hongyi*[1], *ZHU Ruihan*[2], *HE Zhenzong*[2*], *MAO Junkui*[2]

1. AECC Sichuan Gas Turbine Establishment, Mianyang 621000, P.R. China;
2. College of Energy and Power Engineering, Nanjing University of Aeronautics and Astronautics, Nanjing 210016, P. R. China

(Received 9 November 2020; revised 20 January 2021; accepted 22 January 2021)

Abstract: Particles, including soot, aerosol and ash, usually exist as fractal aggregates. The radiative properties of the particle fractal aggregates have a great influence on studying the light or heat radiative transfer in the particle medium. In the present work, the performance of the single-layer inversion model and the double-layer inversion model in reconstructing the geometric structure of particle fractal aggregates is studied based on the light reflectance-transmittance measurement method. An improved artificial fish-swarm algorithm (IAFSA) is proposed to solve the inverse problem. The result reveals that the accuracy of double-layer inversion model is more satisfactory as it can provide more uncorrelated information than the single-layer inversion model. Moreover, the developed IAFSA show higher accuracy and better robustness than the original artificial fish swarm algorithm (AFSA) for avoiding local optimization problems effectively. As a whole, the present work supplies a useful kind of measurement technology for predicting geometrical morphology of particle fractal aggregates.

Key words: inversion radiative problem; artificial fish swarm algorithm; radiative property; particle fractal aggregate; geometrical morphology

CLC number: TK123 **Document code:** A **Article ID:** 1005-1120(2021)01-0057-11

0 Introduction

Particles, including soot, aerosol and ash, usually exist in the form of fractal aggregates, which are suspended in the atmosphere and in industrial equipment, such as combustion chambers and furnaces. The scattering and absorption properties of particles are important factors in the study of heat radiation transfer in industrial equipment and light radiation transfer in the atmosphere. The size distribution, complex refractive index, and morphology of particles have great influence on the scattering and absorption characteristics[1-2]. The optical properties of particles and their interaction with radiation can be reflected by the complex refractive index. As the basic properties of particles, the complex refractive index and particle size distribution are usually considered to be invariant. Many scholars have investigated on the size distribution and complex refractive index of particles using several types of methods[3-9].

The geometrical form of particle and its aggregates is non-essential and easy to change. However, it also has an obvious effect on the radiation properties of particle[10-11]. Accurate inversion of geometric feature parameters becomes more difficult as the soot is aging and evoluting along the direction of flame height, as shown in Fig.1.

The non-invasive measurement method can be realized by optical means, which avoids these problems and proves to be more accurate and effective.

*Corresponding author, E-mail address: hezhenzong@nuaa.edu.cn.

How to cite this article: LIU Zhigang, FANG Hongyi, ZHU Ruihan, et al. Application of light reflectance-transmittance measurement method to reconstruct geometrical morphology of particle fractal aggregates[J]. Transactions of Nanjing University of Aeronautics and Astronautics, 2021, 38(1): 57-67.

http://dx.doi.org/10.16356/j.1005-1120.2021.01.005

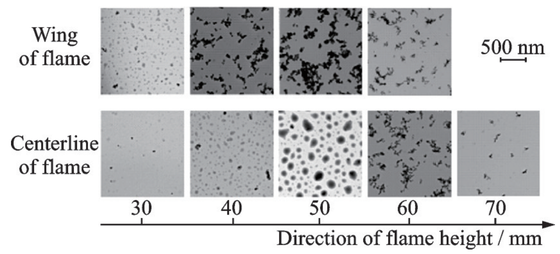

Fig.1 Formation and morphology of soot aggregate in a diffusion flame height[12]

According to the theory of radiation inverse problem, the geometric characteristic parameters of particles can be estimated based on the external radiative transfer signals obtained from the particle medium. In view of the fact that the optical radiation transmission signal can provide a wealth of measurement information such as angle, spectrum and position, different scholars have proposed a variety of methods to reconstruct the geometric characteristics of particles and their fractal aggregates[13-16]. However, the description of the geometric characteristics of the particle fractal aggregates is still a problem that needs to be further studied to improve the accuracy.

The purpose of this paper is to compare two inversion models in reconstructing the geometry of particle aggregates. The improved artificial fish swarm algorithm (IAFSA) is applied to improve the accuracy of the inverse problem. Firstly, the related principles of positive problem, such as fractal aggregate theory, are introduced. Then, AFSA and IAFSA are used to reconstruct the geometric characteristics of fractal aggregates. Finally, the results of this paper are analyzed and the conclusion and prospect are given.

1 Mathematical Model for Direct Problem

1.1 Fractal aggregate theory

As described by the fractal theory (Fig.2), there are several important parameters in describing the morphology and structure of fractal aggregates, i.e., fractal dimension D_f, mean radius of the monomers a, total number of primary monomers N_p, root mean square radius R_g, and fractal prefactor k_f.

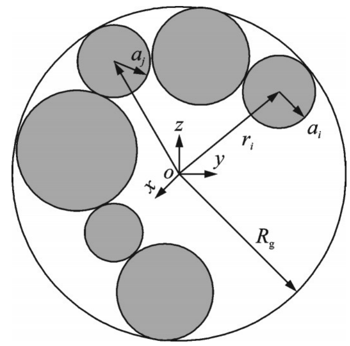

Fig.2 Schematic of fractal-like aggregates

The relationship between these parameters can be described by[17]

$$N_p = k_f \left(\frac{R_g}{a} \right)^{D_f} \tag{1}$$

$$R_g^2 = \frac{1}{N_p} \sum_{i=1}^{N_s} r_i^2 \tag{2}$$

where r_i is the distance from the ith sphere to the center of the aggregate mass. In this paper, R_g conformed to the log-normal (L-N) distribution constructed by Zhang et al.[18] and the volume frequency distributions can be described as

$$f_{\text{L-N}}(R_g) = \frac{1}{\sqrt{2\pi}\, R_g \ln\sigma} \times \exp\left[-\frac{(\ln R_g - \ln R_{g,av})^2}{2(\ln\sigma)^2} \right] \tag{3}$$

where $R_{g,av}$ denotes the characteristic radius; σ the narrowness index. Our previous work[11] reported that N_p, a, D_f and R_g had an important influence on the prediction of the radiation characteristics, while the fractal prefactor had a little one, which can be ignored.

1.2 Light reflectance-transmittance measurement method

When a collimated monochromatic laser beam impinges on the system with particle aggregates at room temperature (Fig.3), the radiative transfer in one-dimension particle system can be described as[1]

$$\boldsymbol{s} \cdot \frac{\partial I_\lambda(z, \boldsymbol{s})}{\partial z} = -(\alpha_\lambda + \sigma_\lambda) I_\lambda(z, \boldsymbol{s}) + \frac{\sigma_\lambda}{4\pi} \int_{4\pi} I_\lambda(z, \boldsymbol{s}_i) \Phi_\lambda(\boldsymbol{s}_i, \boldsymbol{s}) \mathrm{d}\Omega_i \tag{4}$$

where $I_\lambda(z, \boldsymbol{s})$ denotes the spectral radiative intensity in the direction $\boldsymbol{s}$ at location z; l the wavelength of incident laser; α_λ and σ_λ the spectral absorption

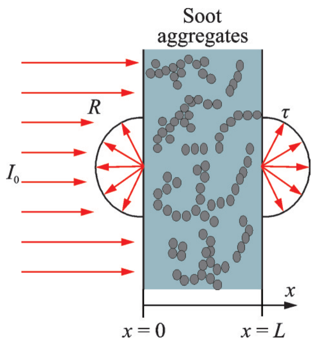

Fig.3 Schematic model of light-scattering measurement methods

and scattering coefficient, respectively; $\Phi_\lambda(\boldsymbol{s}_i, \boldsymbol{s})$ the scattering phase function; and Ω_i the solid angle. α_λ, σ_λ and $\Phi_\lambda(\boldsymbol{s}_i, \boldsymbol{s})$ can be described as

$$\alpha_\lambda = \sum_{i=1}^{n} N(R_{g,i}) C_{abs,\lambda,i}^{agg} \tag{5}$$

$$\sigma_\lambda = \sum_{i=1}^{n} N(R_{g,i}) C_{sca,\lambda,i}^{agg} \tag{6}$$

$$\Phi_\lambda(\boldsymbol{s}_i, \boldsymbol{s}) = \frac{1}{\sigma_\lambda} \sum_{i=1}^{n} N(R_{g,i}) C_{sca,\lambda,i}^{agg} \Phi_{p,i}(\boldsymbol{s}_i, \boldsymbol{s}) \tag{7}$$

where $N(R_{g,i})$ denotes the number concentration of the sample, $N(R_{g,i}) = N_{tot} \times f_{L\text{-}N}(R_{g,i})$; N_{tot} the total number concentration of the sample; $C_{\lambda,sca,i}^{agg}$, $C_{abs,\lambda,i}^{agg}$, and $\Phi_{p,i}$ the scattering cross-section, the absorption cross-section, and the scattering phase function of fractal aggregate. In this paper, the RDG-FA method is applied to estimate the radiative properties of the particle aggregates as it is easy to program. The calculation efficiency is high and the precision is almost the same as that of GMM. The corresponding mathematical expression is[15,19-20]

$$\begin{cases} C_{abs}^{agg} = N_p C_{abs}^{p},\ C_{abs}^{p} = -4\pi k a^3 E(m) \\ E(m) = \mathrm{Im}\left[(m^2-1)/(m^2+2)\right] \end{cases} \tag{8}$$

$$\begin{cases} C_{sca}^{agg} = N_p^2 C_{sca}^{p} G(kR_g) \\ C_{sca}^{p} = \dfrac{8}{3}\pi k^4 a^6 F(m) \\ F(m) = |(m^2-1)/(m^2+2)|^2 \end{cases} \tag{9}$$

$$\begin{cases} C_{vv}^{agg}(\boldsymbol{s}_i, \boldsymbol{s}) = N_p^2 C_{vv}^{p} S(qR_g) \\ C_{vv}^{p} = a^6 k^4 F(m) \end{cases} \tag{10}$$

$$\Phi_p(\boldsymbol{s}_i, \boldsymbol{s}) = \frac{C_{vv}^{agg}(\boldsymbol{s}_i, \boldsymbol{s})}{C_{sca}^{agg}} \frac{1+\cos^2(\boldsymbol{s}_i, \boldsymbol{s})}{2} \tag{11}$$

where $k = 2\pi/\lambda$ denotes the wave number in the vacuum; C_{vv}^{p} the vertical (for incident radiation) and vertical (for scattered radiation) polarized differential scattering cross-section of aggregates; C_{sca}^{p} and C_{abs}^{p} the scattering cross-section and absorption cross-section of monomers; $E(m)$ and $F(m)$ the functions of the complex refractive index m of the monomer; $G(kR_g)$ a generalization function, and its mathematical description is

$$G(kR_g) = \left(1 + \frac{4}{3D_f} k^2 R_g^2\right)^{-D_f/2} \tag{12}$$

$$S(qR_g) = \exp\left[-(qR_g)^2/D_f\right] \times {}_1F_1\left[\frac{3-D_f}{2}, \frac{3}{2}, \frac{(qR_g)^2}{D_f}\right] \tag{13}$$

where $S(qR_g)$ is the aggregate structure factor. As shown in Fig.4, there is a satisfactory agreement between the results obtained by the RDG-FA method and those by the GMM model in predicting the radiation characteristics of fractal aggregates[20-21]. In this paper, the RDG-FA method is used to predict the radiation characteristics of fractal aggregates.

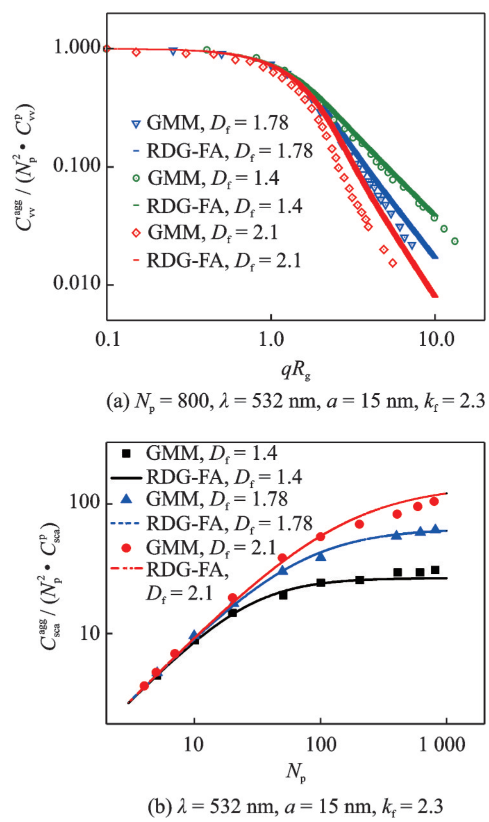

Fig.4 Radiative properties of fractal aggregates predicted by the GMM and RDG-FA methods

The mathematical expression of the boundary condition is

$$I_\lambda^+(0, \theta) = \begin{cases} I_0 & \theta = 0 \\ 0 & 0 < \theta \leqslant \pi/2 \end{cases} \tag{14}$$

$$I_\lambda^-(L,\theta)=0 \quad \pi/2<\theta<\pi \tag{15}$$

where I_0 denotes the total incident light intensity; $I_\lambda^+(0,\theta)$ and $I_\lambda^-(L,\theta)$ the light intensity incident to the internal medium from the light incident side and the light output side of the sample, respectively; L the geometrical thickness of the medium; and θ the polar angle. In this paper, the finite volume method (FVM) is used to simulate the radiation equation because of its good performance in precision and calculation time[22]. The specific implementation process can be referred in Ref.[23]. The mathematical expressions of hemispherical reflectance R and transmittance τ are

$$R=2\pi\int_{\pi/2}^{\pi}\frac{I^-(0,\theta)}{I_0}\cos\theta\sin\theta\mathrm{d}\theta \tag{16}$$

$$\tau=2\pi\int_{0}^{\pi/2}\frac{I^+(L,\theta)}{I_0}\cos\theta\sin\theta\mathrm{d}\theta \tag{17}$$

2 Mathematical Model for Inverse Problem

In water areas, fish can find the place where nutrients are abundant by themselves or by following other fish, so the place where fish usually live most is the place where nutrients are abundant in the water area. Inspired by this phenomenon, the artificial fish-swarm algorithm (AFSA) is applied to solve different problems. There are four operators in the AFSA: preying behavior, swarming behavior, follwing behavior and random behavior, and the state of the individual in the fish group is the vector to be solved. Through the cooperation between the individual fish in the fish group, the problem can be solved. In the algorithm, a bulletin board is usually set up to record the current optimal individual state.

2.1 Standard AFSA

Assuming that the current state of artificial fish individual i is $X_i=(x_{i1},x_{i2},\cdots,x_{in})$, the food concentration of the fish group is set as $Y_i=f(X_i)$, that is, the objective function to be solved, the distance between fish groups can be expressed as $d_{i,j}=\|X_i-X_j\|$, visual is the visual field of fish, δ is the crowding factor, step is the moving step of fish group, and try_number is the number of repeated attempts in foraging behavior. The flow of AFSA is as follows[24-27].

(1) Prey: Assuming that the current state of the fish is X_i, a new state is randomly selected within its field of vision visual($d_{i,j}<d_{\text{visual}}$), as shown in Eq.(18). If $f(X_j)<f(X_i)$, the fish moves one step to the state according to Eq. (19) ; otherwise, choose a new X_j and try again. If the fish maintain its position after trying try_number times, it moves the fish one step at random. n_{Rand1} and n_{Rand2} are random numbers in the range of [0,1].

$$X_j=X_i+d_{\text{visual}}\cdot n_{\text{Rand1}} \tag{18}$$

$$X_i^{t+1}=X_i^t+\frac{X_j-X_i^t}{\|X_j-X_i^t\|}\cdot n_{\text{step}}\cdot n_{\text{Rand2}} \tag{19}$$

where X_i^{t+1} and X_i^t are the artificial fish's next and current state.

(2) Swarm: Assuming that the current state of the fish is X_i, the central position X_c and the number of partners n_f are searched in its field of vision visual. If $Y_c/n_f>\mathrm{d}Y_i$, which means that there are not a lot of fish in the center and there is still a large amount of food there. The fish will take a step in this direction, as shown in Eq.(20). Otherwise, preying behavior will be carried out. n_{Rand3} is a randomly generated number between 0 and 1.

$$X_i^{t+1}=X_i^t+\frac{X_c-X_i^t}{\|X_c-X_i^t\|}\cdot n_{\text{step}}\cdot n_{\text{Rand3}} \tag{20}$$

(3) Follow: Assuming that the fish's current state is X_i, searching partner X_j whose Y_j is the maximum in its field of vision. If $Y_j/n_f>Y_i$, it indicates that there is more food and less fish around the partner X_j, and the fish will thus move forward to that position, otherwise they will continue to prey.

(4) Update the bulletin board: The state of the best fish in history is recorded on a bulletin board. All the artificial fish check their own state every iteration, and if $f(X_j)<f(X_{\text{best}})$, changes X_{best} to X_i.

(5) Random: Assuming that the current state of the fish is X_i, the fish swarm randomly in their own field of vision visual without performing any other behavior.

2.2 Improved AFSA fusing differential evolutionary algorithm

Differential evolutionary algorithm is a kind of evolutionary algorithm proposed by Storn and Price in 1997[27] to solve continuous global optimization problems. Its basic idea is achieved by mutation, crossover and evolution to produce new individuals. Among them, mutation is to weigh the difference between the vectors of two individuals in the population and then sum them with the third individual according to certain rules to produce new individuals. Then, crossover is to combine the new individual with the target individual to produce the probing individual, as shown in Eq.(21). Finally, the probing individual and the original target individual are compared. The original individual will be replaced if its target value is lower than that of the new one; otherwise, it will still be preserved, as shown in Eq.(22)

$$X_{i,\mathrm{mut}} = X_k + F \cdot [X_l - X_m] \tag{21}$$

$$x_{ij,\mathrm{tri}}(t) = \begin{cases} x_{ij,\mathrm{mut}} & \text{if } n_{\mathrm{Rand4}} \leqslant C_{\mathrm{R}} \text{ or } j = Q(i) \\ x_{ij} & \text{if } n_{\mathrm{Rand4}} > C_{\mathrm{R}} \text{ or } j \neq Q(i) \end{cases} \tag{22}$$

where F is a mutation factor between [0,2], i, k, l and m the different individuals in the fish group, C_{R} a cross factor in the range of [0,1], and $Q(i)$ a randomly selected fish group. The flow of AFSA based on differential evolutionary algorithm is as follows:

Step 1 Initialize parameters such as artificial fish size, field of view visual, moving step of fish group step, maximum number of repeated attempts try_number, and the maximum number of iterations.

Step 2 Calculate the objective function of individual fish. Compare it with the value of the bulletin board. Choose the better one to assign to the bulletin board.

Step 3 Each individual fish executes the prey behavior, swarm behavior and follow behavior.

Step 4 Compare the objective functions of the three behaviors and select the optimal values.

Step 5 On the basis of the optimal value selected by Step 4, the difference approximation is carried out, and the objective function of the probing individual and the target individual is calculated. Compare values with that of the bulletin board. Choose the best one to assign to the bulletin board.

Step 6 Check the termination conditions, if a predetermined number of evolutions or a predetermined objective value is reached, then output the optimal solution (artificial fish state and function value in bulletin board). The algorithm terminates, otherwise, turn to Step 3.

3 Numerical Simulation

3.1 Single-layer inverse model

The objective function value F_{obj} is defined as the sum of the squared residuals of the ratio between the estimated signals ratios and the measured signals ratios. The lower the objective function value is, the closer the result is to the real value. Therefore, the geometric parameters are inversed by minimizing F_{obj}.

$$F_{\mathrm{obj}} = \frac{1}{2}\left[\left(\frac{R_{\mathrm{est}} - R_{\mathrm{mea}}}{R_{\mathrm{mea}}}\right)^2 + \left(\frac{\tau_{\mathrm{est}} - \tau_{\mathrm{mea}}}{\tau_{\mathrm{mea}}}\right)^2\right] \tag{23}$$

In order to reduce the certain randomness of the stochastic optimization, all the inversion results have been calculated for $N=30$. The reliability and feasibility of the optimization algorithm is evaluated by the following characteristic parameters:

(1) The relative deviation ξ, which means the sum of the deviation between the probability distribution predicted by the IAFSA and the true distribution of R_{g}, can be expressed as

$$\xi = \frac{\left\{\sum_{i=1}^{N'}[f_{\mathrm{est}}(\widetilde{R}_{\mathrm{g},i}) - f_{\mathrm{true}}(\widetilde{R}_{\mathrm{g},i})]^2\right\}^{1/2}}{\left\{\sum_{i=1}^{N'}[f_{\mathrm{true}}(\widetilde{R}_{\mathrm{g},i})]^2\right\}^{1/2}} \tag{24}$$

where N' is the number of subintervals that the size range $[R_{\mathrm{g,min}}, R_{\mathrm{g,max}}]$ is divided; $\widetilde{R}_{\mathrm{g},i}$ the midpoint of the i th subinterval $[R_{\mathrm{g},i}, R_{\mathrm{g},i+1}]$; $f_{\mathrm{true}}(\widetilde{R}_{\mathrm{g},i})$ the true distribution in the i th subinterval; and $f_{\mathrm{est}}(\widetilde{R}_{\mathrm{g},i})$ the predicted distribution in the i th subinterval.

(2) The standard deviation η and the relative error δ here are defined as

$$\begin{cases} \eta_X = \sqrt{\dfrac{1}{N}\sum_{i=1}^{N}(\bar{X}_{\mathrm{est}} - X_{\mathrm{est},i})^2} \\ \bar{X}_{\mathrm{est}} = \dfrac{1}{N} \times \sum_{i=1}^{N} X_{\mathrm{est},i} \\ X = D_{\mathrm{f}}, R_{\mathrm{g}}, R_{\mathrm{g,av}} \text{ or } \sigma \end{cases} \tag{25}$$

$$\begin{cases}\delta_X = \dfrac{\left|\bar{X}_{\mathrm{est}} - X_{\mathrm{real}}\right|}{X_{\mathrm{real}}} \\ X = D_{\mathrm{f}}, R_{\mathrm{g}}, R_{\mathrm{g,av}} \text{ or } \sigma\end{cases} \tag{26}$$

where $\bar{X}_{\mathrm{est}}$ and X_{real} denote the average values of estimated results and the real value of the parameters, respectively.

3.1.1 Comparison of standard AFSA and IAFSA

The performance of IAFSA can be investigated by comparing with that of AFSA. Table 1 lists the parameters of different algorithms. In this paper, when one of the following conditions are met, the algorithm is terminated: the maximum number of generations is equal to 1 000 or the iteration accuracy is less than 10—16. Table 2 lists the results of different algorithms when (D_{f}, R_{g})=(1.8, 80). Table 2 shows that the results obtained by IAFSA are more accurate than that of the AFSA in the inversion of D_{f} and R_{g}, regardless of adding random measurement errors. And the performance of the two algorithms in inversion of fractal dimension R_{g} is more satisfactory than that in inversion of radius of revolution D_{f}. However, even with 5% measurement error added, the inverse results of D_{f} and R_{g} are acceptable. The values of the objective function between AFSA and IAFSA are compared in Fig.5. It is easy to find that the convergence properties of the IAFSA algorithm are better than those of the AFSA algorithm, which means that the IAFSA is of higher efficiency and accuracy in terms of the application of inversion.

Table 1 System control parameters of the AFSA algorithms

Parameter	Visual	Step	Try_number	F	C_{R}
AFSA	30	0.3	10	0.5	0.2
IAFSA	30	0.3	10	—	—

Table 2 Results retrieved by different AFSA algorithms when (D_{f}, R_{g})=(1.8,80)

Algorithm	Parameter	Measurement error		
		0	3%	5%
AFSA	($\bar{D}_{\mathrm{f}}$, $\bar{R}_{\mathrm{g}}$)	(1.766, 80.27)	(1.965, 79.23)	(2.003, 77.69)
	($\delta_{D_{\mathrm{f}}}$, $\delta_{R_{\mathrm{g}}}$)	(0.019, 0.003)	(0.091, 0.009)	(0.113, 0.029)
	($\eta_{D_{\mathrm{f}}}$, $\eta_{R_{\mathrm{g}}}$)	(0.102, 0.694)	(0.418, 3.271)	(0.537, 4.197)
IAFSA	($\bar{D}_{\mathrm{f}}$, $\bar{R}_{\mathrm{g}}$)	(1.800, 79.99)	(1.825, 79.84)	(1.833, 79.35)
	($\delta_{D_{\mathrm{f}}}$, $\delta_{R_{\mathrm{g}}}$)	(0.0, 0.000 1)	(0.014, 0.002)	(0.018, 0.008)
	($\eta_{D_{\mathrm{f}}}$, $\eta_{R_{\mathrm{g}}}$)	(0.002, 0.017)	(0.117, 1.783)	(0.271, 3.594)

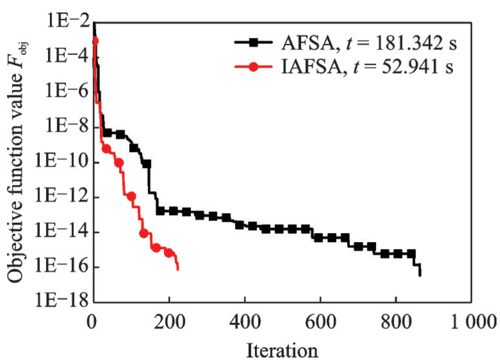

Fig.5 Comparison of objective function values of AFSA and IAFSA

The accuracy of inverse results is affected to a certain extent by the multi-value of the results. It means there are more than one result satisfying the convergence conditions at the end of inversion calculation. Thus, the accuracy of inversion results is reduced. As far as this paper is concerned, multi-value includes the same experimental hemispherical reflectance R and transmittance τ corresponding to many couples of (D_{f}, R_{g}), which means a unique solution may not be found in the inverse problem. Fig.6 depicts the distribution of objective functions in the single-layer model. As can be seen from the graph of the objective function, multiple points on a curve are in the minimum region. Comparing the inverse results of D_{f} and R_{g}, it can be found that the inversion accuracies of D_{f} and R_{g} are different even without random measurement error. As can be seen from Fig.6, the range of D_{f} that meets the convergence conditions covers the whole inversion range [1,3], while the range of R_{g} that meets the convergence conditions is only in the range of [75,90]. It means the retrieval results for D_{f} are worse than those for R_{g} as the multi-value characteristics are

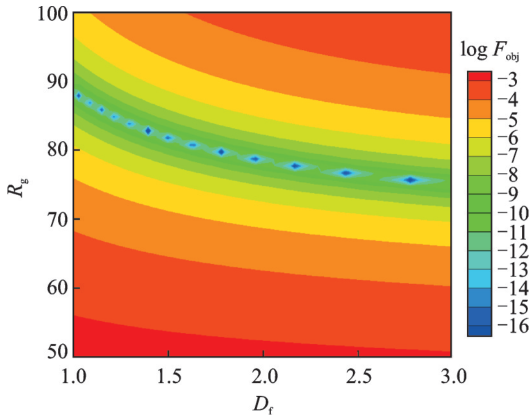

Fig.6 Distribution of objective function value under single-layer inverse model

more serious.

3.1.2 Retrieval of geometrical characteristic parameters of particle fractal aggregates

Table 3 lists the results retrieved by the single-layer model when R_g obeying L-N distribution. Their true values are set as $(N_p, D_f, R_{g,av}, \sigma, a)=(60, 1.7, 117, 2.1, 10)$. The inversion accuracy decreases with the increase of random measurement error. And the relative errors δ and standard errors η increase accordingly. Fig.7 depicts the retrieval curves of the probability density distribution $f_{L\text{-}N}(R_g)$ of the root mean square radius R_g in different cases. The black dot symbols represent the real value curve, the red box represents the retrieval curve for inversion of three parameters, the blue triangle represents the retrieval curve for inversion of four parameters, and the green triangle represents the retrieval curve for inversion of five parameters. It can be found that the inversion accuracy decreases as the number of inversion parameters increases.

Table 3 Results retrieved by single-layer model when R_g obeying L-N distribution

Real value	Parameter	Measurement error		
		0	1%	3%
Case 4 $(D_f, R_{g,av}, \sigma)=(1.7, 117, 2.1)$	$(\bar{D}_f, \bar{R}_{g,av}, \bar{\sigma})$	(1.751, 113.2, 2.144)	(1.774, 110.8, 2.181)	(1.810, 108.8, 2.242)
	$(\delta_{D_f}, \delta_{R_{g,av}}, \delta_\sigma)$	(0.031, 0.032, 0.021)	(0.044, 0.053, 0.039)	(0.065, 0.071, 0.068)
	$(\eta_{D_f}, \eta_{R_{g,av}}, \eta_\sigma)$	(0.163, 2.225, 0.051)	(0.194, 3.115, 0.116)	(0.242, 4.717, 0.196)
	ξ	0.050 791	0.086 935	0.129 895
Case 5 $(N_p, D_f, R_{g,av}, \sigma)=(60, 1.7, 117, 2.1)$	$(\bar{N}_p, \bar{D}_f, \bar{R}_{g,av}, \bar{\sigma})$	(58.49, 1.871, 113.7, 2.183)	(55.56, 1.917, 110.3, 2.258)	(50.74, 1.934, 125.5, 1.957)
	$(\delta_{N_p}, \delta_{D_f}, \delta_{R_{g,av}}, \delta_\sigma)$	(0.025, 0.101, 0.028, 0.039)	(0.074, 0.128, 0.057, 0.075)	(0.154, 0.138, 0.073, 0.068)
	$(\eta_{N_p}, \eta_{D_f}, \eta_{R_{g,av}}, \eta_\sigma)$	(0.251, 0.129, 2.158, 0.016)	(0.277, 0.127, 4.144, 0.185)	(0.474, 0.100, 6.654, 0.246)
	ξ	0.066 118	0.125 828	0.140 958
Case 6 $(N_p, D_f, R_{g,av}, \sigma, a)=(60, 1.7, 117, 2.1, 10)$	$(\bar{N}_p, \bar{D}_f, \bar{R}_{g,av}, \bar{\sigma}, \bar{a})$	(50.63, 1.905, 110.3, 2.218, 10.98)	(48.64, 1.933, 109.3, 2.319, 10.95)	(42.53, 1.985, 128.8, 2.574, 11.56)
	$(\delta_{N_p}, \delta_{D_f}, \delta_{R_{g,av}}, \delta_\sigma, \delta_a)$	(0.156, 0.121, 0.057, 0.056, 0.098)	(0.189, 0.137, 0.065, 0.104, 0.095)	(0.291, 0.167, 0.101, 0.226, 0.156)
	$(\eta_{N_p}, \eta_{D_f}, \eta_{R_{g,av}}, \eta_\sigma, \eta_a)$	(2.87, 0.218, 6.651, 0.237, 1.567)	(3.85, 0.160, 4.450, 0.248, 1.682)	(4.88, 0.135, 5.328, 0.225, 1.061)
	ξ	0.107 523	0.160 251	0.207 183

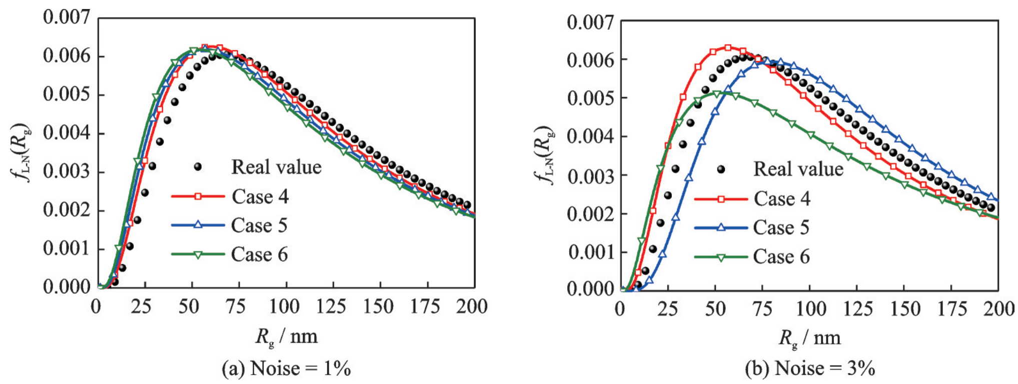

Fig.7 Retrieval curves of root mean square radius using different measurement methods

When only three parameters are inverted, the inverse accuracies of results are acceptable even with 3% random measurement error, and the maximum relative error is only 7.1%. The inversion accuracy decreases with more parameters retrieved. Under 3% random measurement error, the maximum relative errors of N_p, D_f, $R_{g,av}$ and σ inversion results are 15.4%, 13.8%, 7.3% and 6.8%, respectively. At the same time, the inversion results deteriorate gradually when five parameters are retrieved. When 1% random measurement error is added, the relative errors of N_p and D_f are large, being 18.9% and 13.7%, respectively. The inversion results of $R_{g,av}$, σ, and a are better, and the standard deviation is controlled within 11%.

3.2 Double-layer inverse model

The predicted results of the geometrical characteristic parameters are satisfactory without random errors. However, the accuracy of inversion decreases gradually as random errors are added. The reason may be that only a couple of the reflectance and transmittance signals can be obtained, while more than two characteristic parameters, i. e. the mean radius of the monomers a, total number of primary monomers N_p, and the root mean square radius R_g, need to be retrieved. To solve this problem and improve the inverse accuracy, the double-layer inverse model, which can provide more useful information about the particle medium, is used in this paper. Two thicknesses of the layers are used (L_1= 0.02 m, L_2=0.04 m). The true values of them are set as $(N, D_f, R_{g,av}, \sigma, a)=(60, 1.7, 117, 2.1, 10)$. And the objective function F_{obj} is

$$F_{obj}=\frac{1}{4}\times\left[\left(\frac{R_{est,1}-R_{mea,1}}{R_{mea,1}}\right)^2+\left(\frac{\tau_{est,1}-\tau_{mea,1}}{\tau_{mea,1}}\right)^2\right]+\frac{1}{4}\times\left[\left(\frac{R_{est,2}-R_{mea,2}}{R_{mea,2}}\right)^2+\left(\frac{\tau_{est,2}-\tau_{mea,2}}{\tau_{mea,2}}\right)^2\right] \tag{27}$$

Table 4 lists the results retrieved by using the double-layer inverse model when R_g obeying L-N distribution. Fig.8 shows the distribution of the distribution of objective functions in the double-layer model. Fig.9 shows that the overall trend of the estimation results using the double-layer model is consistent with that of the single-layer model. When the random measurement errors are not added, the calculation results are better. While inverse results become worse when the random measurement error added increase. As the number of simultaneous inversion parameters increases, the accuracy of calcu-

Table 4 Results retrieved by double-layer inverse model when R_g obeying L-N distribution

Real value	Parameter	Measurement error: 0	1%	3%
Case 9 $(D_f, R_{g,av}, \sigma)=(1.7, 117, 2.1)$	$(\bar{D}_f, \bar{R}_{g,av}, \bar{\sigma})$	(1.669, 116.2, 2.114)	(1.753, 113.3, 2.127)	(1.801, 111.8, 2.168)
	$(\delta_{D_f}, \delta_{R_{g,av}}, \delta_\sigma)$	(0.018, 0.007, 0.007)	(0.031, 0.032, 0.013)	(0.059, 0.053, 0.032)
	$(\eta_{D_f}, \eta_{R_{g,av}}, \eta_\sigma)$	(0.134, 1.859, 0.014)	(0.337, 5.366, 0.046)	(0.371, 6.051, 0.059)
	ξ	0.013 072	0.042 667	0.072 991
Case 10 $(N_p, D_f, R_{g,av}, \sigma)=(60, 1.7, 117, 2.1)$	$(\bar{N}_p, \bar{D}_f, \bar{R}_{g,av}, \bar{\sigma})$	(60.63, 1.877, 114.6, 2.123)	(61.72, 1.947, 114.6, 2.171)	(62.86, 1.881, 110.1, 2.213)
	$(\delta_{N_p}, \delta_{D_f}, \delta_{R_{g,av}}, \delta_\sigma)$	(0.011, 0.104, 0.021, 0.011)	(0.029, 0.145, 0.021, 0.034)	(0.047, 0.107, 0.059, 0.054)
	$(\eta_{N_p}, \eta_{D_f}, \eta_{R_{g,av}}, \eta_\sigma)$	(0.441, 0.131, 3.135, 0.077)	(0.563, 0.225, 5.709, 0.162)	(0.821, 0.206, 7.033, 0.214)
	ξ	0.029 906	0.054 061	0.106 822
Case 11 $(N_p, D_f, R_{g,av}, \sigma, a)=(60, 1.7, 117, 2.1, 10)$	$(\bar{N}_p, \bar{D}_f, \bar{R}_{g,av}, \bar{\sigma}, \bar{a})$	(63.86, 1.871, 111.6, 2.111, 10.67)	(65.43, 1.836, 113.7, 1.985, 11.09)	(52.95, 1.838, 106.5, 1.965, 10.69)
	$(\delta_{N_p}, \delta_{D_f}, \delta_{R_{g,av}}, \delta_\sigma, \delta_a)$	(0.064, 0.101, 0.046, 0.005, 0.067)	(0.091, 0.080, 0.028, 0.055, 0.109)	(0.117, 0.081, 0.089, 0.064, 0.069)
	$(\eta_{N_p}, \eta_{D_f}, \eta_{R_{g,av}}, \eta_\sigma, \eta_a)$	(16.84, 0.183, 7.131, 0.274, 2.072)	(13.73, 0.181, 5.445, 0.256, 1.295)	(16.58, 0.173, 7.254, 0.318, 1.116)
	ξ	0.052 951	0.072 453	0.114 535

Note: The mean and standard deviation of the 30 times retrieval results are shown in the form of $x \pm y$.

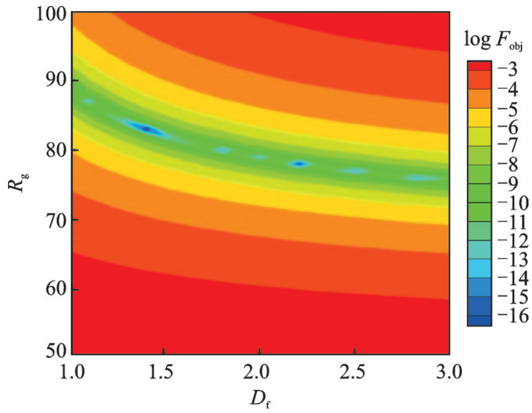

Fig.8 Distribution of objective function value under double-layer inverse model

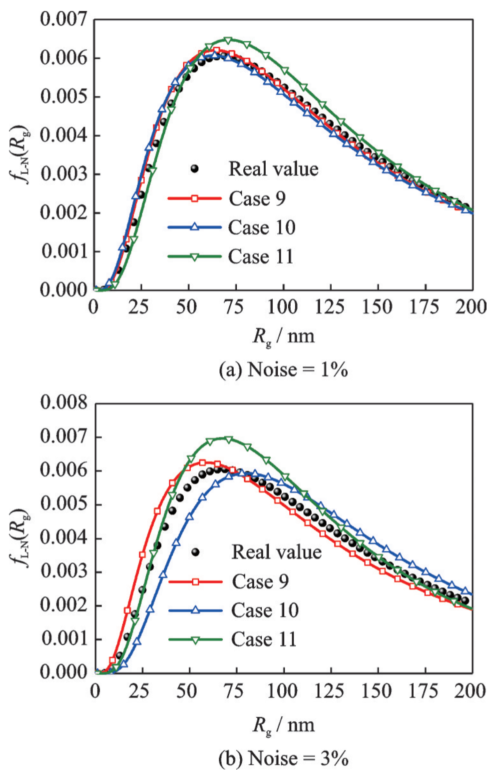

Fig.9 Retrieval curves of root mean square radius using the measurement angles with different intervals

lation results decreases.

Compared Fig.6 with Fig.8, it can be found that when the objective function value arrives at $10e^{-16}$ in the single-layer-inverse model, the regions of the objective function value tend to different points, which means the retrieval results are not unique. While the double-layer inverse model is applied, the multiplicity of the inverse results will be decreased, and just a few points satisfy the objective function value equal to $10e^{-16}$. When the random errors added to the measurement signals, the objective function value may not arrive at the convergence limit. For example, with 3% random error added to the measurement signals, the objective function value can only reach $10e^{-12}$. From Figs.6, 8, it can be found that the region of the objective function value less than $10e^{-12}$ in single-layer-inverse model is larger than that in double-layer inverse model, which means more couples of characteristic parameters in single-layer-inverse model that meet objective function value equal to $10e^{-12}$. The phenomenon can explain why more satisfactory retrieval results are obtained in double-layer inverse model. Specifically, the inversion results of five parameters are satisfactory even when the random measurement noise is increased by 3%. Its relative error is generally less than 10%. Only the inversion result of N_p is slightly worse, its relative error is 11.7%. Compared with the results obtained by the single-layer model, it has a considerable improvement. This is because using the double-layer model can provide more useful information about fractal aggregates than using the single-layer one.

4 Conclusions

Based on the IAFSA, this paper investigates the robustness and reliability of two inverse model in reconstructing the geometrical characteristic parameters of fractal aggregates. The conclusions are as follows:

(1) When retrieving the geometric parameters of fractal aggregates, IAFSA is more accurate than AFSA, and its calculation speed is faster.

(2) With the increase of the number of simultaneous inversion parameters, the inversion accuracy gradually decreases. However, the inversion results are still satisfactory even with 3% random measurement error.

(3) Compared with the single-layer inverse model, the retrieval results obtained by the double-layer inverse model show better convergence accuracy and robustness as the double-layer inverse model is more effective to avoid the multi value characteristics of retrieval results and improve the accuracy of inversion results.

In conclusion, the IAFSA and the double-layer inverse model are effective and reliable in reconstructing the geometric structure of fractal aggregates.

References

[1] MODEST M F. Radiative heat transfer[J]. Journal of Heat Transfer, 1993, 135(6): 061801.

[2] MISHCHENKO M I. Scattering, absorption, and emission of light by small particles[M]. Cambridge, UK: Cambridge University Press, 2002.

[3] HE Zhenzong. Non-parametric estimation of particle size distribution from spectral extinction data with PCA approach[J]. Powder Technology, 2018(325): 510-518.

[4] YUAN Y, YI H L, SHUAI Y, et al. Inverse problem for aerosol particle size distribution using SPSO associated with multi-lognormal distribution model[J]. Atmospheric Environment, 2011, 45(28): 4892-4897.

[5] REN Tatao, QI Hong, CHEN Qin, et al. Simultaneous retrieval of the complex refractive index and particle size distribution[J]. Optics Express, 2015, 23(15): 19328-19337.

[6] HE Zhenzong , MAO Junkui, HAN Xinsi, et al. Retrieval of aerosol optical constants from angular light-scattering measurement signals using principal component analysis approach[J]. Particuology, 2019(43): 210-218.

[7] MAO Qianjun, ZHANG Yamei. Thermal energy storage performance of a novel three-PCM cascade tank in a high-temperature packed bed system[J]. Renewable Energy, 2020(152): 110-119.

[8] XU Yamin, SHEN Jianqi, CAI Xiaoshu, et al. Particle size analysis by transmission fluctuation spectrometry with band-pass filters[J]. Powder Technology, 2008, 184(3): 291-297.

[9] ZHANG W W. Particle size distribution recovery in dynamic light scattering by optimized multi-parameter regularization based on the singular value distribution[J]. Powder Technology, 2019(353): 320-329.

[10] LIU L, ARNOTT W P. A study of radiative properties of fractal soot aggregates using the superposition T-matrix method[J]. Journal of Quantitative Spectroscopy and Radiative Transfer, 2008, 109(15): 2656-2663.

[11] HE Zhenzong, DONG Chuanhui, LIANG Dong, et al. A weighted-sum-of-gray soot-fractal-aggregates model for nongray heat radiation in the high temperature gas-soot mixture[J]. Journal of Quantitative Spectroscopy and Radiative Transfer, 2021(260): 107431.

[12] MOHAMMAD R K, YASHAR A, ANTON D S, et al. Comparison of multiple diagnostic techniques to study soot formation and morphology in a diffusion flame[J]. Combustion and Flame, 2017, 176(2): 567-583.

[13] PATIENCE G, OTMAR S, HAROLD J, et al. Comparison of three methods of fractal analysis applied to soot aggregates from wood combustion[J]. Journal of Aerosol Ence, 2006, 37(7): 820-838.

[14] MAO Qianjun. Recent developments in geometrical configurations of thermal energy storage for concentrating solar power plant[J]. Renewable and Sustainable Energy Reviews, 2016(59): 320-327.

[15] SORENSEN C M. Light scattering by fractal aggregates: A review[J]. Aerosol Science and Technology, 2001.

[16] SORENSEN C M, YON J, LIU Fengshan, et al. Light scattering and absorption by fractal aggregates including soot[J]. Journal of Quantitative Spectroscopy and Radiative Transfer, 2018(217): 459-473.

[17] XU Yulin, NIKOLAI G K. Orientation-averaged radiative properties of an arbitrary configuration of scatterers[J]. Journal of Quantitative Spectroscopy and Radiative Transfer, 2003(79): 1121-1137.

[18] ZHANG Junyou, QI Hong, WANG Yifei, et al. Retrieval of fractal dimension and size distribution of non-compact soot aggregates from relative intensities of multi-wavelength angular-resolved light scattering[J]. Optics Express, 2019, 27(2): 1613-1631.

[19] LIU Fengshan, CECILLIA W, DAVID R S, et al. Investigation of absorption and scattering properties of soot aggregates of different fractal dimension at 532 nm using RDG and GMM[J]. Aerosol Science and Technology, 2013, 47(12): 1393-1405.

[20] SORENSEN C M, CAI J, LU N. Test of static structure factors for describing light scattering from fractal soot aggregates[J]. Langmuir, 1992, 8(8): 2064-2069.

[21] HE Zhenzong, QI Hong, REN Yatao, et al. Application of the time-domain and frequency-domain radiative measurement signals in retrieving the spectral complex refractive index of microalgae[J]. International Journal of Hydrogen Energy, 2017, 42(15): 10591-10603.

[22] SUBHASH C M, PRANSHU C, PRANAV K, et al. Development and comparison of the DTM, the DOM and the FVM equations for the short-pulse laser

transport through a participating medium[J]. International Journal of Heat and Mass Transfer, 2006, 49 (11/12): 1820-1832.

[23] WANG Chujiao, XIA Shixiong. Application of probabilistic causal-effect model based artificial fish-swarm algorithm for fault diagnosis in mine hoist[J]. Journal of Software, 2010, 5(5): 474-481.

[24] WANG Cuiru, ZHOU Chunlei, MA Jianwei. An improved artificial fish-swarm algorithm and its application in feed-forward neural networks[C]//Proceedings of International Conference on Machine Learning & Cybernetics. [S.l.]: IEEE, 2005.

[25] DING Xianyun, ZHU Yu. Segmentation for sem image based on two-dimensional entropy and artificial fish swarm algorithm[J]. Laser and Infrared, 2010, 40(2): 210-214.

[26] FARZI S. Efficient job scheduling in grid computing with modified artificial fish swarm algorithm[J]. 2009, 1(1): 13-18.

[27] STORN R, PRICE K. Differential evolution: A simple and efficient heuristic for global optimization over continuous spaces[J]. Journal of Global Optimization, 1997, 11(4): 341-359.

Acknowledgements This work was supported by the National Natural Science Foundation of China (No. 51806103), the Natural Science Foundation of Jiangsu Province (No. BK20170800) , and the Aeronautical Science Foundation of China (No. 201928052002). A very special acknowledgement is made to the editors and referees who make important comments to improve this paper.

Authors Mr. **LIU Zhigang** is a staff of Sichuan Gas Turbine Establishment. His research is focused on heat transfer of gas turbine.

Dr. **HE Zhenzong** received his Ph.D. degree in engineering thermophysics from Harbin Institute of Technology in 2016. He is currently an associate professor in Nanjing University of Aeronautics and Astronautics. His research is focused on the radiative heat transfer of high gas and soot in the aero-engine combustion chamber, soot size inversion prediction and fuel cell system.

Author contributions Mr. **LIU Zhigang** contributed to the discussion and analysis as well as prepared all drafts, and draw all the figures. Mr. **FANG Hongyi** and Mr. **ZHU Ruihan** contributed to the discussion and analysis. Dr. **HE Zhenzong** contributed to design of the study and wrote the manuscript. Prof. **MAO Junkui** contributed to background, discussion and analysis of the study.

Competing interests The authors declare no competing interests.

(Production Editor: ZHANG Tong)

光反射-透射测量方法在颗粒分形聚集体几何形貌重建中的应用

刘志刚[1], 方弘毅[1], 朱瑞韩[2], 贺振宗[2], 毛军逵[2]

(1.中国航发四川燃气涡轮研究院,绵阳 621000, 中国; 2.南京航空航天大学能源与动力学院,南京 210016, 中国)

摘要:颗粒态物质通常以分形聚集形式存在,如碳烟、气溶胶和灰尘。颗粒分形聚集体辐射特性对研究颗粒介质中光热辐射传输有重要影响。基于光反射-透射测量方法,分析比较了单层反演模型和双层反演模型对重构颗粒分形聚集体几何特征参数的影响,并发展了一种改进的人工鱼群算法作为反问题方法,旨在提高反演结果精度。研究表明,双层反演模型比单层反演模型能提供更多的不相关信息来提高反演精度。与人工鱼群算法相比,改进的人工鱼群算法具有更高的精度和更好的鲁棒性,能够有效地避免局部优化问题。本文结果为预测颗粒分形聚集体几何特征参数提供了一种有效的测量技术。

关键词:反辐射问题;人工鱼群算法;辐射特性;颗粒分形聚集体;几何形貌